Tribology International 42 (2009) 373–377

Contents lists available at ScienceDirect

Tribology International

journal homepage: www.elsevier.com/locate/triboint

A coupled finite element and meshfree analysis of erosive wear

Yu-Fei Wang, Zhen-Guo Yang *

Department of Materials Science, Fudan University, Shanghai 200433, China

ARTICLE INFO

Article history:
Received 2 August 2007
Received in revised form
13 June 2008
Accepted 18 July 2008
Available online 3 September 2008

Keywords:
Erosion model
Meshfree
Smoothed particle hydrodynamics (SPH)
Finite element method (FEM)

ABSTRACT

Erosive wear is a kind of material degradation, which is largely involved in many industries, and caused a series of serious problems and economic loss. Many theoretical models and numerical models have been established to study the erosion phenomena. In this study, a coupled finite element and meshfree model was developed for the simulation and prediction of erosive wear. By utilizing the meshfree technique, the error due to mesh distortion and tangling at impacted area in the finite element analysis could be effectively avoided. The fundamental mechanisms of erosion by solid particle impact were investigated as well. Comparison against the results of analytical erosion models and finite element model are made. It is shown that the predicted results are in agreement with reported results. The present study could be very useful and efficient in studying erosive wear.

1. Introduction

In many industries, such as transport, marine, offshore, process, aeronautical and mining, power station, petrochemical plant, etc., there is a regular requirement for components such as valves, pumps, pipework, extrusion dyes, powder mixers, turbines and helicopter blades to perform in aggressive environments, which are erosive [1]. Erosive wear is a dynamic process that causes material degradation and shortens the service life to the components. Bitter [2] defined erosion as "material damage caused by the attack of particles entrained in a fluid system impacting the surface at high speed". Generally, removal of materials on erosive wear is involved in different mechanisms [3]: cutting and chip formation for ductile metals and polymers; crack formation and brittle fracture for ceramics, glasses and brittle polymers; tearing and fatigue for rubbers.

Since the erosion phenomenon is important and complicated, it has been studied extensively [4–10]. Some analytical models and prediction equations have been obtained and reported through experimental methods [11]. Analytical models have limited applications because these models and equations usually require experimental constants and cannot be extended to cover all materials, coatings and erosion parameters [12]. In recent years the finite element (FE) models have been developed to study the erosion process. The 2-D simulation [13–17] has advantages of fine meshes and less computation time. However, it has to obey certain assumption such as plane strain, plane stress or axisymmetric model, and the multi-particle erosion effect is difficult to be modeled. The 3-D model [12,18–22] also has limitation such as the coarseness of the 3-D grid would affect the accuracy of the result. Moreover, for the erosion under middle and low particle speed, the traditional FE models could normally simulate the erosive behavior. As for the high speed erosion, the great kinetic energy of erodent particles may make Lagrange meshes of the impacted area distortion during large deformation. Some studies [23,24] used Euler or Arbitrary Lagrange–Euler (ALE) meshes to fix the problem. However, the element failure and erosion rate could not be given by Euler or ALE meshes.

In recent years, the meshfree methods have been developed for specific applications [25–27]. In these methods, the domain of interest is discretized by a scattered set of particles. The meshfree methods have a number of advantages over other methods of processing in that it is gridless and therefore there are no mesh tangling problems, as in the standard Lagrange methodology. So these methods are ideal for hp-adaptivity, fracture problems and large deformation problems. However, the meshfree methods are usually more expensive in computation time than FEM. Thus, several mixed FEM and meshfree methods have been proposed [28–31] to use the advantages of each method. In the current study, the cumulative damage model with the coupling algorithm of smoothed particle hydrodynamics (SPH) [32] scheme and FE mesh was used. The impacted area with fracture is modeled by the SPH, while the other section with less deformation uses FE discretisation. The effect of impact angle and impact velocity on the target material as well as the crater depth, residual stresses after impact and the energy transformation were discussed.

* Corresponding author. Tel.: +86 2165642523; fax: +86 2165103056.
E-mail address: zgyang@fudan.edu.cn (Z.-G. Yang).

0301-679X/$ - see front matter © 2008 Elsevier Ltd. All rights reserved.
doi:10.1016/j.triboint.2008.07.009

2. Modeling

The erosive processes are simulated using a 3-D explicit dynamic analysis within ANSYS/LS-DYNA. The Johnson–Cook (J–C) [33,34] viscoplastic material model with Grüneisen equation of state (EOS) was employed to model the flow stress behavior of the target Ti-6Al-4V material. Johnson and Cook express the von Mises flow stress as detailed in Eq. (1):

$$\sigma = (A + B\varepsilon^n)(1 + c \ln \dot{\varepsilon}^*)(1 - T^{*m}) \quad (1)$$

where A and B are yield stress constant and strain hardening constant; n, c, m are constants; and ε is the equivalent plastic strain, $\dot{\varepsilon}^* = \dot{\varepsilon}/\dot{\varepsilon}_0$ is the dimensionless plastic strain rate for $\dot{\varepsilon}_0 = 1.0\,\text{m/s}$. $T^* = (T - T_r)/(T_m - T_r)$, T, T_r and T_m are the target material temperature, room temperature and melting point of the target material, respectively.

A shear failure model is utilized to model the failure: the damage occurs when the damage parameter $D = \sum \Delta\varepsilon/\varepsilon_f$ reaches the value of 1. $\Delta\varepsilon$ is the incremental plastic strain per computational cycle, and the failure strain ε_f is given by

$$\varepsilon_f = (d_1 + d_2 \exp d_3\sigma^*)(1 + d_4 \ln \dot{\varepsilon}^*)(1 + d_5 T^*) \quad (2)$$

where σ^* is the dimensionless pressure–stress ratio and d_1–d_5 are experimental constants determined from compressive split Hopkinson bar tests.

The Grüneisen EOS is adapted for the ductile solid materials. The cubic shock velocity v_s and particle velocity v_p are related by

$$v_s = C_0 + Sv_p \quad (3)$$

where C_0 is the intercept of the v_s–v_p curve and S is the coefficient of the slope of the v_s–v_p curve.

The material constants for Ti-6Al-4V alloy are detailed in Table 1. The erodent is 500-μm steel sphere particles with a density of 7890 kg/m^3. Five-particle FE model was employed to calculate the erosion rate. In the computer simulation, the particles are modeled as rigid bodies to save CPU time.

Totally 1000 SPH particles were used in modeling the impacted section at the target center. The uniform mass of each SPH particle was 3.5424×10^{-11} kg. The other section of the target was meshed by the eight-node linear brick hexahedral elements with one integration point. The tied_nodes_to_surface contact was established between the SPH scheme and FE mesh in order to couple the SPH and FE section. Also, the eroding_nodes_to_surface contact was defined between every impacting particle and the SPH section. There is no contact defined among the impacting particles. The solution time is set to $1.5 \times t_5$, where t_5 is the time when the last particle contacted to the target surface.

Only a half-model was evaluated, so the constrains and SPH symmetry plane were set for the FE and SPH sections at the boundaries to achieve the symmetry conditions. All of the bottom and outside nodes of the target materials were defined for non-reflecting boundaries. The SPH scheme and FE mesh of the erosion model are shown in Fig. 1.

Generally, the erosion rate (mg/g) was used to characterize the erosion performance of the target materials. It is defined as

$$\text{Erosion rate} = \frac{\text{Cumulative mass loss of target materials(mg)}}{\text{Impact particles weight (g)}} \quad (4)$$

In this study, the variation of impact angle and impact velocity in the model was achieved through ANSYS Parametric Design Language (APDL). The impact angle varies from 15° to 90° in increments of 15°. The impact velocity varies from 60 to 105 m/s in increments of 15 m/s.

Table 1
Material constants of ductile materials [35–37]

Materials properties	Symbol	Ti-6Al-4V
Density	ρ (kg/m^3)	4428
Shear modulus	G (GPa)	41.9
Poisson's ratio	v	0.31
J–C yield strength	A (MPa)	862
J–C hardening coefficient	B (MPa)	331
J–C strain hardening exponent	n	0.34
J–C strain rate constant	c	0.012
J–C softening exponent	m	0.80
Melting temperature	T_m (K)	1878
Specific heat	C_p (J/kg K)	580
J–C damage constant	d_1	−0.09
J–C damage constant	d_2	0.27
J–C damage constant	d_3	0.48
J–C damage constant	d_4	0.014
J–C damage constant	d_5	3.87
Elastic bulk wave velocity	C_0 (km/s)	5.13
Slope in v_s versus v_p diagram	S	1.028
Grüneisen coefficient	γ_0	1.23

3. Results and discussion

For the solid particle erosion on ductile materials such as metals and alloys, as shown in Fig. 2, material removal is caused

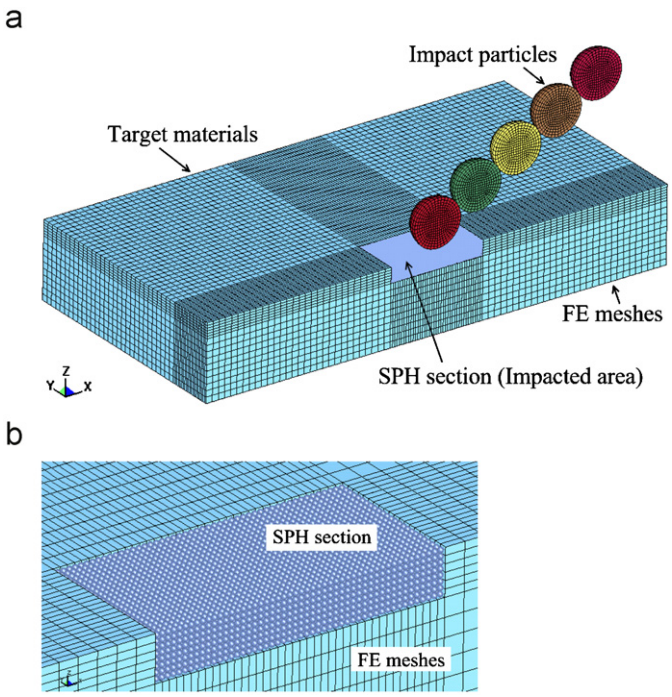

Fig. 1. Numerical model of erosive wear at 30° impact angle: (a) FE mesh section and (b) SPH section at center of the target material.

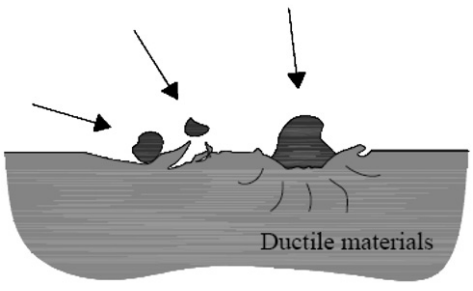

Fig. 2. The erosive failure behavior of ductile materials.

by the micro-cutting and micro-ploughing processes in which the material reveals a large plastic deformation at the impacted location. Fig. 3 shows the plastic strain of the target material after erosion with 30° and 90° impact angle at 75 m/s. The plastic deformation at 90° impact angle is greater than the situation at 30°, but the weight loss at 90° impact angle is less than the situation at 30° The cumulative mass losses by erosion at 30 and 90° impact angles are shown in Fig. 4. The erosion rates are given by calculating the slopes of the curves. Fig. 5 shows the simulation results of erosion rate (as a function of the impact angle) as well as the analytical results by Bitter's model [2,7] and FE results in the literature [21]. The maximum erosion rate appeared when the solid particles obliquely impacted the target materials. This phenomenon has been approved by lots of experiments and tests [38].

The relationship between erosion rate and the impact velocity has also been discussed through the model. For metallic materials, the erosion rate is proportional to the *N*th-power of the impact velocity, and the value is within 2.05–2.44 [6]. Yerramareddy and Bahadur [39] found the value for Ti-6Al-4V alloy is 2.35 by the experiment at 30° impact angle with 120 grit silicon carbide

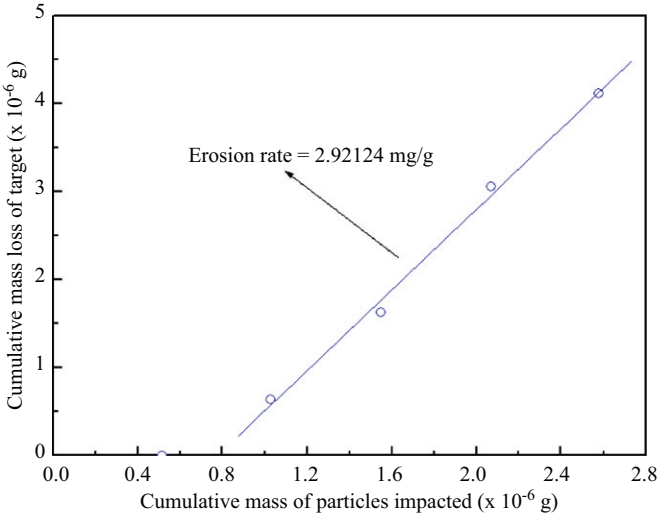

Fig. 4. Variation of erosive mass loss with mass of impacting particles.

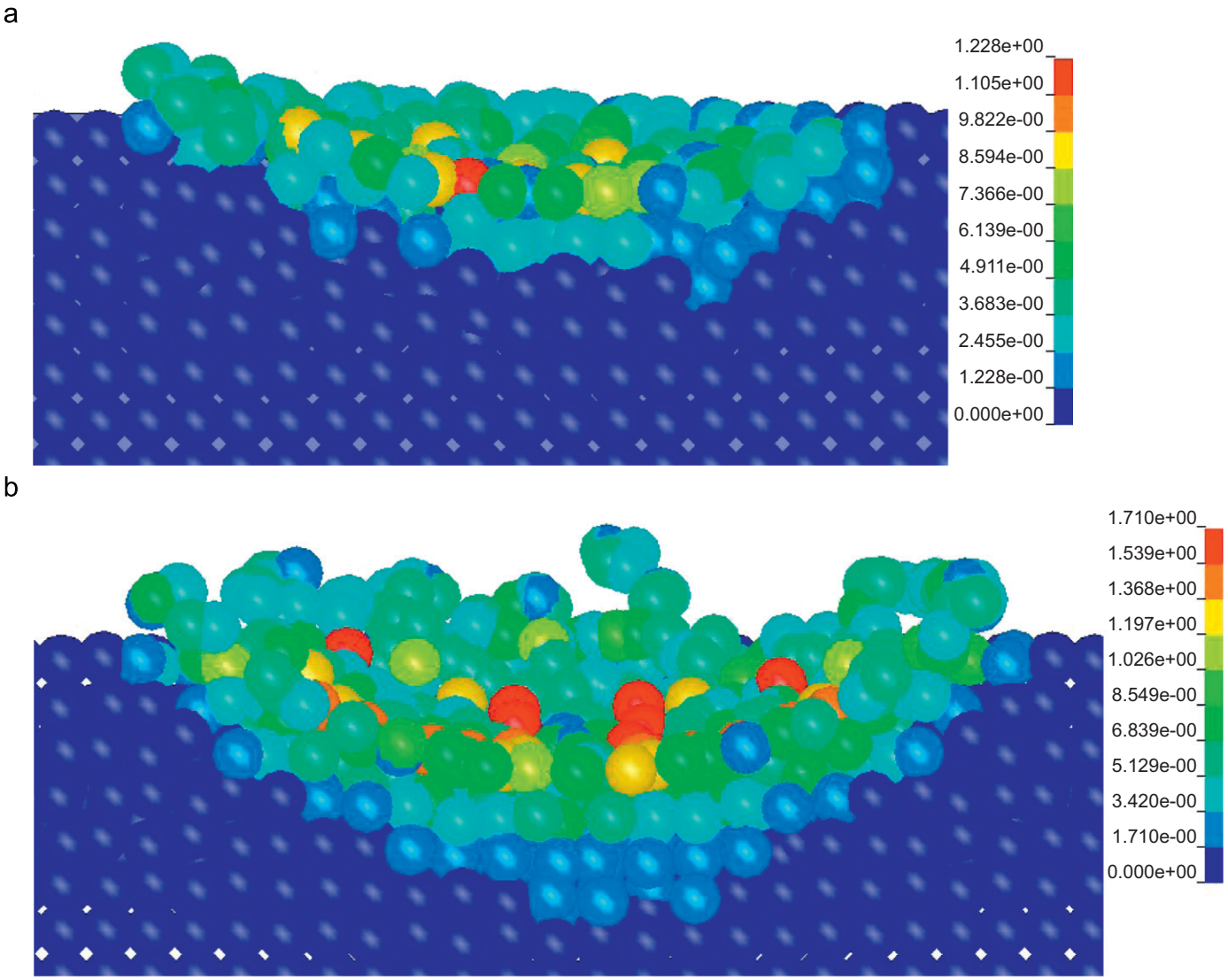

Fig. 3. The erosive plastic strain on the target material: (a) at 30° impact angle and (b) at 90° impact angle.

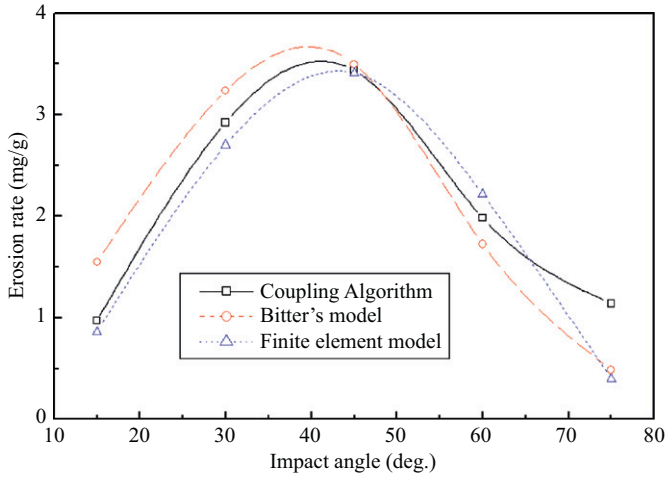

Fig. 5. Variation of erosion rate with impact angle for ductile materials.

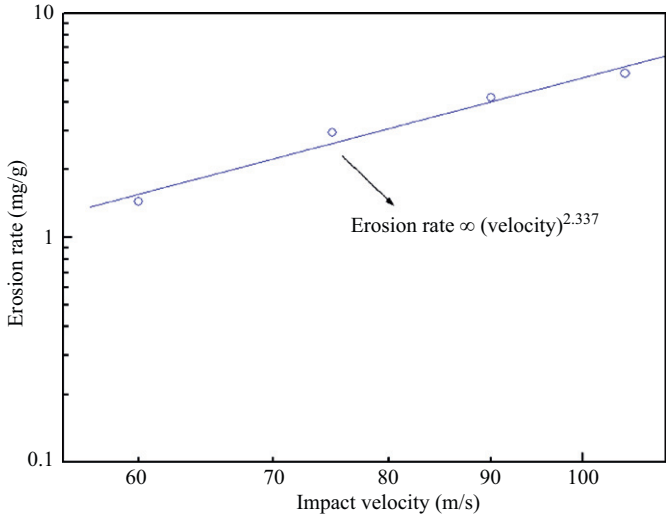

Fig. 6. Variation of erosion rate with the impact velocity for ductile materials.

erodent. Fig. 6 shows the simulated results of variation of erosion rate with the impact velocities on log–log coordinates. The slopes of the straight lines fitted through the data points provide the exponent N equal to 2.337. This value of exponent falls within the corresponding ranges.

For ductile materials, despite the maximum erosion rate is at oblique impact angle, the crater depth increases as the angle increases as shown in Fig. 7. Higher normal component of the velocity causes greater plastic deformation with lower material removal. This has also been validated by the study of Shimizu et al. [14].

Due to the high-speed impingement of particles, there are residual stresses in the impacted materials, which are difficult to investigate by experimental methods. Fig. 8 gives the residual stress, σ_x, in the X direction after five-particle normal impact, along the path defined from the top node to the bottom node. There are certain compressive residual stresses at the impacted surface and the new surface after the failed elements removal. The residual stress magnitude increases below the surface until reaching a maximum at a certain depth and then tend to decrease, transforming into low-magnitude tensile residual stresses. The similar results were also given in the previous FE analyses [21,22].

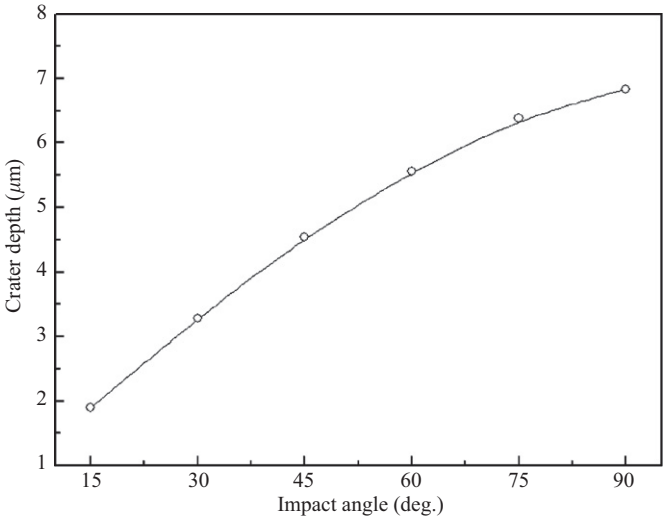

Fig. 7. Variation of crater depth with impact angle.

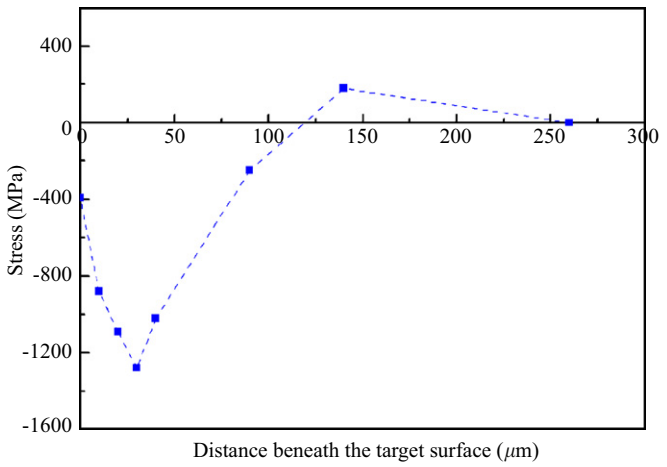

Fig. 8. The residual stress (σ_x) profiles after five-particle impact.

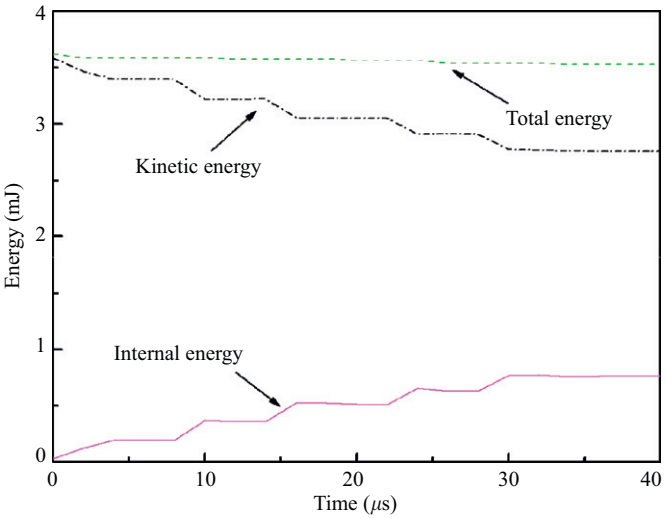

Fig. 9. Variation of global energy with time (half-model).

After impact, the kinetic energy of the impact particles is transferred to the target, and as the erosion takes place, the kinetic energy will be reduced while the internal energy of the

system will increase. Distributions of global kinetic, internal and total energy with respect to time are shown in Fig. 9. It should be noted that only a half of the system energy is represented because only a half of the spatial domain is considered. It is observed that the kinetic energy reduces as the particles impacting the target while the internal energy increases. While the total energy in any physical system is conserved, the slightly dissipation of the total energy is the result of the mass loss of the target material during the erosion process. Fawaz et al. [40] gave the similar trend in the study of ballistic impacting on ceramic composite armours.

4. Conclusions and considerations

A new erosion model based on coupling algorithm of SPH and FEM was developed in the study. The error due to mesh distortion and tangling at impacted area in the FE simulation could be avoided utilizing this numerical model. The major impact factors of erosive wear such as impact angle, impact velocity, residual stresses as well as the crater depth and the energy transformation are successfully calculated. Its results are in good agreement with the analytical and experimental data. The present study could be very useful and efficient in studying erosive wear.

Acknowledgements

The authors are grateful to the financial support of this research Project no. 052912049 by Science and Technology Commission of Shanghai Municipality, PR China, and Shanghai Leading Academic Discipline Project (Project no. B113).

References

[1] Wood RJK. The sand erosion performance of coatings. Mater Des 1999; 20:179–91.
[2] Bitter JGA. A study of erosion phenomena part I. Wear 1963;6:5–21.
[3] Lancaster JK. Material-specific wear mechanisms: relevance to wear modeling. Wear 1990;141:159–83.
[4] Hutchings IM. Particle erosion of ductile metals: a mechanism of material removal. Wear 1974;27:121–8.
[5] Stachowiak GW, Batchelor AW. Engineering tribology. 2nd ed. Wohurn: Butterworth-Heinemann; 2000. p. 509–23.
[6] Finnie I. Erosion of surfaces by solid particles. Wear 1960;3:87–103.
[7] Bitter JGA. A study of erosion phenomena part II. Wear 1963;6:169–90.
[8] Hutchings IM. Ductile–brittle transitions and wear maps for the erosion and abrasion of brittle materials. J Phys D: Appl Phys 1992;25:A212–21.
[9] Finnie I, Stevick GR, Ridgely JR. The influence of impingement angle on the erosion of ductile metals by angular abrasive particles. Wear 1992;152:91–8.
[10] Barkoula N-M, Karger-Kocsis J. Review processes and influencing parameters of the solid particle erosion of polymers and their composites. J Mater Sci 2002;37:3807–20.
[11] Meng HC. Wear modeling: evaluation and categorization of wear models. PhD thesis, University of Michigan, Ann Arbor, MI, 1994.
[12] Griffin D, Daadbin A, Datta S. The development of a three-dimensional finite element model for solid particle erosion on an alumina scale/MA956 substrate. Wear 2004;256:900–6.
[13] Shimizu K, et al. FEM analysis of the dependency on impact angle during erosive wear. Wear 1999;233–235:157–9.
[14] Shimizu K, et al. FEM analysis of erosive wear. Wear 2001;250:779–84.
[15] Chen Q, Li DY. Computer simulation of solid particle erosion. Wear 2003; 254:203–10.
[16] Chen Q, Li DY. Computer simulation of erosion–corrosion of a non-passive alloy using a micro-scale dynamic model. Mater Sci Eng A 2004;369:284–93.
[17] Li W-Y, et al. Numerical simulation of deformation behavior of Al particles impacting on Al substrate and effect of surface oxide films on interfacial bonding in cold spraying. Appl Surf Sci 2007;253:5084–91.
[18] Woytowitz PJ, Richman RH. Modeling of damage from multiple impacts by spherical particles. Wear 1999;233–235:120–33.
[19] Molinari JF, Ortiz M. A study of solid-particle erosion of metallic targets. Int J Impact Eng 2002;27:347–58.
[20] Zouari B, Touratier M. Simulation of organic coating removal by particle impact. Wear 2002;253:488–97.
[21] ElTobgy MS, Ng E, Elbestawi MA. Finite element modeling of erosive wear. Int J Mach Tool Manuf 2005;45:1337–46.
[22] Wang Y-F, Yang Z-G. Finite element model of erosive wear on ductile and brittle materials. Wear 2008;265:871–8.
[23] Aquaro D, Fontani E. Erosion of ductile and brittle materials. Meccanica 2001;36:651–61.
[24] Aquaro D. Erosion due to the impact of solid particles of materials resistant at high temperature. Meccanica 2006;41:539–51.
[25] Babuska I, Melenk JM. The partition of unity method. Int J Numer Meth Eng 1996;40:727–58.
[26] Belytschko T, Liu YY, Gu L. Element-free Galerkin methods. Int J Numer Meth Eng 1994;37:229–56.
[27] Liu WK, Jun S, Zhang YF. Reproducing kernel particle methods. Int J Numer Meth Fluids 1995;20:1081–106.
[28] Belytschko T, Organ D, Kronggauz Y. A coupled finite element-element-free Galerkin method. Comput Mech 1995;51:221–58.
[29] Liu WK, Uras RA, Chen Y. Enrichment of the finite element method with reproducing kernel particle methods. J Appl Mech 1997;64:861–70.
[30] Huera A, Fernandez-Mendez S. Enrichment and coupling of the finite element and meshless methods. Int J Numer Mech Eng 2000;48:1615–36.
[31] Wu C-T, Botkin ME, Wang H-P. Development of a coupled finite element and mesh-free method in LS-DYNA. In: 7th international LS-DYNA users conference, Dearborn, MI, May 2002. p. 1229–40.
[32] Gingold RA, Monaghan JJ. Smoothed particle hydrodynamics: theory and application to non-spherical stars. Mon Not R Astron Soc 1977;181:375–89.
[33] Johnson GR, Cook WH. A constitutive model and data for metals subjected to large strains, high strain rates and high temperatures. In: Proceedings of the 7th international symposium on ballistics, The Hague, 1983. p. 541–7.
[34] Johnson GR, Cook WH. Fracture characteristics of three metals subjected to various strains, strain rates, temperatures and pressures. Eng Fract Mech 1985;21:31–48.
[35] Leseur DR. Experimental investigations of material models for Ti-6Al-4V titanium and 2024-T3 aluminum. Technical report DOT/FAA/AR-00/25, US Department of Transportation, Federal Aviation Administration, 2000.
[36] Kay G. Failure modeling of titanium 6Al-4V and aluminum 2024-T3 with the Johnson–Cook material model. Technical Report DOT/FAA/AR-03/57, US Department of Transportation, Federal Aviation Administration, 2003.
[37] Steinberg DJ. Equation of state and strength properties of selected materials, Lawrence Livermore national laboratory report. UCRL-MA-106439, Livermore, CA, 1996.
[38] Hutchings IM. A model for the erosion of metals by spherical particles at normal incidence. Wear 1981;70:269–81.
[39] Yerramareddy S, Bahadur S. Effect of operational variables, microstructure mechanical properties on the erosion of Ti-6Al-4V. Wear 1991;142:253–63.
[40] Fawaz Z, Zheng W, Behdinan K. Numerical simulation of normal and oblique ballistic impact on ceramic composite armours. Compos Struct 2004;63: 387–95.